Clays and Clay Minerals, Vol. 55, No. 1, 18–35, 2007.

CLAY MINERALOGY AND CHEMISTRY OF HALLOYSITE AND ALUNITE DEPOSITS IN THE TURPLU AREA, BALIKESIR, TURKEY

Ö. Işik Ece[1,2,*] and Paul A. Schroeder[1]

[1] The University of Georgia, Department of Geology, Athens, GA 30602-2501, USA
[2] Istanbul Technical University, Faculty of Mines, Department of Geological Sciences, Mineralogy-Petrography Division, Maslak 34469 Istanbul, Turkey

Abstract—A field-mapping and crystal-chemical study of two alunite- and halloysite-rich deposits in the Turplu area, situated northwest of Balıkesir on the Biga Peninsula of northwest Turkey reveals a mineralogically diverse and a potentially economic clay deposit. The mineral assemblage along fault zones is dominated by halloysite and sometimes alunite. The alunite is nearly end-member in composition (a = 6.995 Å, c = 17.195 Å) often occurring with a minor Ca phosphate phase. Of the two deposits studied, the more northerly mine contains more alunite relative to halloysite. Geochemical alteration indices suggest that the northern mine has experienced a slightly greater degree of hydrothermal modification. Halloysite is found in both hydrated and dehydrated states and assumes a tubular morphology. Observations by transmission and scanning electron microscopy are consistent with a model of halloysite dehydration, where the shapes transform from an open-hole tubular morphology to a closed-hole unfurled morphology.

Mineral paragenesis includes the effects of initial deposition of volcanic tuffs and andesite on top of karstic terrain. The contact between altered volcanics and underlying limestones is irregular and appears to have provided a mechanism to flush both hydrothermal and meteoric waters through the volcanics. Periods of hydrothermal alteration (hypogene) contemporaneous with extensional and strike-slip faulting have resulted in alunite and halloysite deposits. Hydrothermal alteration is concentrated near the fault zones. Because of subsequent weathering (supergene) away from the fault zones, much of the andesitic volcanic rocks have been altered to a more smectite-rich and kaolinite-bearing assemblage. The deposits continue to be both plastically deformed in the alunite/halloysite regions and to undergo brittle deformation in the saprolitized volcanics. Tectonic deformation has mixed the contacts, such that limestone blocks are entrained into parts of the alteration zones. Gibbsite and gypsum are common weathering products associated with limestone block inclusions. Genetic models for the origins of alunite-halloysite deposits in NW Turkey should consider as possible influencing factors the underlying lithologies, the extent of hydrothermal alteration, and recent weathering by meteoric fluids. In the case of the Turplu deposits, karstic limestones, hydrothermal circulation of sulfate-rich waters, and a post-alteration history of meteoric weathering were all important factors in their formation.

Key Words—Acid-sulfate Thermal Waters, Alunite Deposits, Biga Peninsula, CryoSEM, Geochemistry, Halloysite Deposits, HRTEM, Hydrothermal Alteration, Hypogene *vs*. Supergene, SEM.

INTRODUCTION

High-purity halloysite [$Al_2Si_2O_5(OH)_4 \cdot 2H_2O$] and alunite [$KAl_3(SO_4)_2(OH)_6$] deposits are a valuable resource because they provide Al- and K-rich sources for industrial materials (*e.g.* ceramics, cements and fertilizers) and structural templates for nanotechnology engineering (Joussein *et al*., 2005). Northwestern Turkey hosts several halloysite and alunite deposits that can help in the development of genetic models for their geological origin. The purpose of this study is to examine two proximal halloysite and alunite deposits in the Turplu area, situated northwest of Balıkesir on the Biga Peninsula of northwest Turkey (see Figure A1: all figures and tables prefaced by an A are available from the 'Deposited Material' section of The Clay Minerals Society's website: www.clays.org/journal/JournalDeposits.html). The focus is to characterize the mineral assemblages in terms of morphological and textural relations, crystallography and chemistry towards developing a framework to explain the origin and distribution of halloysite and alunite, which can lead to the economic viability of similar deposits.

The two halloysite/alunite deposits studied here are located along the contact between metamorphic rocks of the Triassic Karakaya Complex and lower Miocene volcanics (Genç, 1998). The mid−late Cenozoic tectonic regime of Turkey is characterized by continental collision between the Eurasian and Arabian plates. The Anatolian Block moved westward along the North Anatolian Fault zone (NAF), which is now a 1200 km long left-lateral strike-slip fault (Figure A1: www.clays.org/journal/JournalDeposits.html) that also marks the boundary between the Eurasian and Anatolian plates (Okay *et al.*, 1991, 1999). The rate of movement along the NAF is reduced in the Aegean region and tectonic

* E-mail address of corresponding author:
ece@itu.edu.tr
DOI: 10.1346/CCMN.2007.0550102

deformation is manifested in N−S extension and E−W compression (Okay *et al.*, 2000). The geological history of the Aegean region, as recorded by Miocene stratigraphy, can be described as an extensional tectonic regime characterized by deposition of calc-alkaline tuffs, ashes and pyroclastic rocks ejected along NE−SW-trending fractures and faults. These NE−SW *en-echelon* faults constitute the western segments of the NAF zone in the Biga Peninsula. Regional fault trends are represented by the (1) Manyas-Danışment fault in the southeast, (2) the Yenice-Gönen fault in the middle and (3) the Sarıköy-Inova fault in the northwest (Figure A1: www.clays.org/journal/JournalDeposits.html). Our study site is located in the southern part of the Manyas-Danışment fault zone.

The Kocadere River flows along a strike-slip fault zone which is thought to have formed during the tectonic uplifting of the Karakaya Complex. It has been postulated that reverse and strike-slip faulting in the Karakaya Complex are coeval with granite-granodiorite shallow-level emplacement during the early Miocene (Genç, 1998; Altunkaynak and Yilmaz, 1998, 1999). These tectonic and more recent climatic factors make the study area ideal for studying the anatomy of halloysite/alunite deposits because the active extensional tectonics have rapidly exhumed these fossil hydrothermal systems. Sparse vegetative cover and mining activities allow good exposure of the deposits.

The hydrothermally altered halloysite/alunite deposits in the Turplu area constitute the largest known in the Balya-Yenice-Gönen region. The study area is shown in Figure 1, which is a geological map produced from our field reconnaissance. A large halloysite deposit is being exploited at the intersection of N85ºE/60ºSE and N20ºE/70ºNW-trending normal faults along the Kocadere River west of Turplu (H in Figure 1). A smaller alunite-

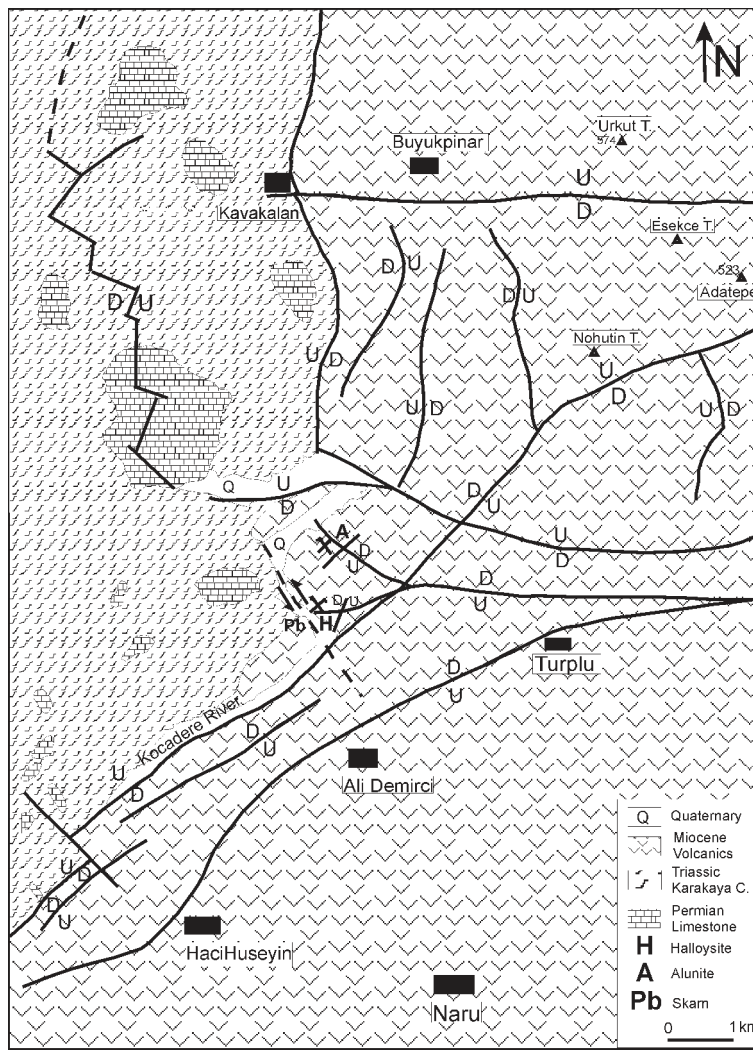

Figure 1. Geological map of the study area at Turplu Mine, Balıkesir. The solid lines show fault zones with relative displacement (U/D) and the dashed line indicates a strike-slip fault zone along the Kocadere River.

Figure 2. General view of the southern halloysite mine. Hydrothermal mineralization occurred at the intersection of the N20ºE (left) and N85ºE (right) fault zones. D/U shows the relative displacement of the normal fault. V = volcanics, Ls = limestone terrain.

bearing deposit is also being exploited for lesser amounts of halloysite and is located ~1 km to the north (A in Figure 1). Its distribution is coincident with a N50ºW and N60ºE-trending normal fault. The estimated areas of mineralization of the southern and northern mines are 300 m × 400 m and 200 m × 400 m, respectively. Each deposit base contact undulates due to the deposition of lavas, tuffs and ashes on pre-existing karstic topography. Some 200 m to the west of the Kocadere River there is a very small zone of skarn-type galena-chalcopyrite mineralization within Permian carbonate rocks (Pb in Figure 1).

METHODS

Sampling and field relations

Field sampling was based on reconnaissance using local base maps and global positioning system (GPS) locations. Standard geological field procedures were used for identifying lithologies and structures (Freeman, 1999). Clay deposits are best exposed inside valleys along hill slopes which are cut by small faults oriented quasi-perpendicular to the Kocadere River (Figures 1 and 2).

Several sample suites were employed, with the first including a representative collection of unaltered volcanics and altered volcanics composed of alunite, 'hydrated' halloysite, and 'dehydrated' halloysite. The terms in inverted commas are defined here based on physical appearances in the field. 'Hydrated' halloysite appears as lustrous pearly white to light yellow to light pink nodules. 'Dehydrated' halloysite under sunlight appears pasty or powdery white and surrounded by small fractures. Alunite resembles white porcelain in hand specimen. It is harder than the kaolin and less powdery than the nodules.

A second series of samples was collected across fault zones, going from within centrally located, highly altered fault zones into the surrounding less-altered volcanics. A third suite constitutes samples taken from the southern mine across a 2 m transect that included an altered andesite that transitions into an almost pure halloysite (samples T-64 to T-68, Figure 3). The purpose of these last two sampling strategies is to provide a general sense of zonation for clay mineral assemblages that result either from higher-temperature hydrothermal process or from lower-temperature weathering processes.

Analytical procedures

The major elements of selected samples were determined by means of a Rigaku® 3070 X-ray fluorescence spectrometer using the techniques described by Ece and Nakagawa (2003). Trace elements and rare earth elements (*REE*) of all samples were

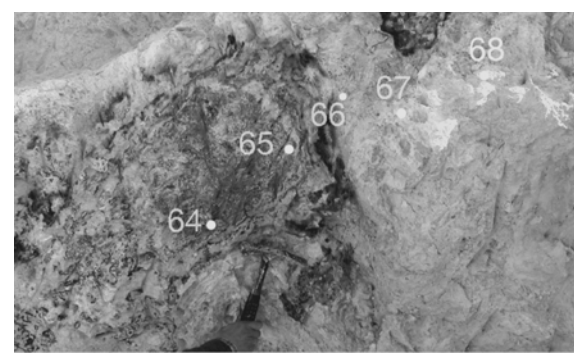

Figure 3. Concentric exfoliation texture of altered andesitic tuffs. Liesigang banding proceeds from the core (T-64) to the most altered region of almost pure halloysite (sample T-68). Corresponding chemical data are given in Table A3, and Figures 4A and 15.

determined by inductively coupled plasma optical emission spectrometry techniques (Ece and Nakagawa, 2003). The extent of alteration was assessed through analysis of change in concentration of elements relative to the parent rocks (Altaner *et al.*, 2003; Grant, 1986; Gresens, 1967). Methods employed included using elemental data normative *REE* plots and a chemical alteration index ($\%\Delta_i$), where i is the element of interest.

$$\%\Delta_i = \frac{\left[\left(\frac{C^{P}_{Al_2O_3} C^{D}_{i}}{C^{D}_{Al_2O_3}}\right) - C^{P}_{i}\right]}{C^{P}_{i}} x100 \quad (1)$$

Changes are relative to Al, which is assumed to be conserved under both hydrothermal and weathering conditions. In equation 1, $C^{P}_{Al_2O_3}$ = Al_2O_3 concentration in the parent rock; $C^{D}_{Al_2O_3}$ = Al_2O_3 concentration in the altered rock; C^{P}_{i} = concentration of i in the parent rock; and C^{D}_{i} = concentration of i in the altered rock.

A Scintag® XDS 2000 model powder X-ray diffractometer was used for mineralogical studies. The instrument parameters included using a Co radiation source. Samples were ground for XRD analysis using a McCrone® micronizing mill to reduce the particle-size distribution to <10 μm. The Sonifier® cell disruptor 350 model ultrasonic instrument was used to disaggregate clay particles for better size separation before X-ray diffraction (XRD) analyses. Intercalation complexes were used to differentiate dehydrated halloysite from kaolinite. Intercalation was accomplished using the formamide (FM) and dimethyl sulfoxide (DMSO) tests (Churchman *et al.*, 1984; Churchman, 1990; Theng *et al.*, 1984).

Differential thermogravimetric analysis (DTGA) was conducted on a Hi-Res® TGA 2950 model instrument. Nitrogen was used as the purging gas. About 14 mg of sample powder were loaded in a platinum sample holder and then transferred onto a scale in the furnace. Initial heating was set at 30ºC with a heating rate of 10ºC/min up to 900ºC in a helium atmosphere (the rate varies when weight loss occurs and the weight stabilizes). Differential thermal analysis (DTA) was performed using a Perkin-Elmer® DTA-7 thermal analysis system at a heating rate of 10ºC/min in an argon atmosphere. The chemical composition of the alunite samples was examined in thin-sections using a Jeol® JXA-8600 model superprobe with wavelength dispersive spectrometer using a 15 keV, 5 nA beam current and beam diameter of 10 μm.

The effects of vacuum on the morphology of hydrated halloysite during Au-Pd coating processes and SEM studies have not been studied in great detail. In order to minimize vacuum-induced artifacts, Cryo-SEM and freeze fracture replica transmission electron microscopy (TEM) sample preparation techniques were employed (Bozzola and Russell, 1999). Hydrated halloysite and oven-dried halloysite samples were compared using both SEM and TEM studies. Morphological and textural features of various clays were examined using an Leo® 982 model field emission scanning electron microscope (FE-SEM). An SPI-Module® sputter coater was used for Au-Pd alloy coating under operating conditions of 2 mbar, 15 mA and 50 s. This provided a ~150 Å thick coating. For Cryo-SEM studies, halloysite samples were mounted onto a commercial Gatan Alto® 2500 cryostage and cryoprep chamber and held in place with Tissue-Tek® (Bozzola and Russell, 1999). The sample was then plunged into nitrogen slush (−209ºC) to avoid the Leidenfrost effect. The frozen sample was quickly transferred to an Alto® 2500 model cryo-preparation unit attached to the FE-SEM and allowed to sublimate at a vacuum of 2×10^{-6} torr and −80ºC for 2 min to remove frost on the surface. The sample was brought back down to −100ºC before coating with Au-Pd to a thickness of 30 nm. Once coated, the sample was transferred to a −100ºC cold stage in the FE-SEM for viewing.

The relationship between particle-size distribution and morphology was studied with an FEI-Technai® 20 model TEM. Clay slurries were prepared by dilution in distilled water and dispersion in an ultrasonic bath for 10 min. Formvar-covered polymer micro grids were plunged into the clay slurry and dried at room temperature and provided optimal sample mounting. Samples were then loaded onto 3 mm diameter gold planchets and rapidly plunged into liquid propane maintained with liquid nitrogen at ~−192ºC. Each gold planchet was then transferred to a multi-planchet holder in liquid nitrogen until it could be loaded into the Balzers® freeze fracture device. The sample was fractured and sublimated at −100ºC for 20 s and then coated with platinum at an angle of 35º for 7 s. This was followed by carbon evaporation for 10 s. The sample was removed from the freeze fracture device and the replica was floated onto 50 wt.% glycerol. The sample was subsequently transferred to 10 wt.% glycerol and finally washed twice in in deionized water. Samples were then floated onto 70 wt.% bleach (or concentrated HCl, HF acid) and left for 3 days in a humid chamber to remove remaining sample from the replicas. The replicas were washed several times in deionized water and mounted on 400 mesh copper grids to be viewed using a Jeol® 100 CX model TEM.

RESULTS

X-ray diffraction analysis shows that the deposits comprise a mineral assemblage that mainly includes 10 Å and 7 Å halloysite, but also feldspars, quartz, goethite, gibbsite, alunite, smectite and illite. Core−rim Fe staining is a common feature in larger exfoliations of andesitic tuffs found in both mines. The XRD analysis and field observations also reveal pyrite, realgar,

cinnabar, orpiment, azurite, bornite, chalcopyrite, psilomelane, hematite, gypsum, and other clays are sometimes associated with halloysite and alunite mineralization. Pyrite is mostly concentrated within the fault clays with small amounts of chalcopyrite. Arsenic and Cu sulfides are irregularly distributed in very small discontinuous bands in the clay body. Very thin and discontinuous gibbsite-rich zones occur between halloysite and large limestone blocks. The limestone blocks range from 3 m^3 to 5 m^3 in size and are sometimes surrounded by 10–20 cm thick Fe and Mn hydroxide (goethite and psilomelane) bands. Also, gypsum bands are found on the surface of limestone blocks and infilling micro fractures in the blocks to a depth of ~20 cm.

Mineral and chemical nature of halloysite and alunite

Representative XRD patterns of halloysite-rich samples obtained under ambient relatively humidity (~50%) are shown in Figure 4. Halloysite is identified by a basal peak at ~10 Å (expanded with water, FM or DMSO), ~7 Å (dehydrated), and its disordered 020 reflection which appears in the range of 4.41 to 4.46 Å. Most samples display a mixture of varying percentages of expanded and collapsed halloysite layers. 'Dehydrated' halloysites display a broad diffraction peak at ~7.3 Å that sharpens upon heating to 60ºC (T-89, Figure 4). The halloysite d_{020} measures at 4.45 Å under ambient relative humidity and shifts to 4.42 Å upon heating. The basal reflections for both 'hydrated' and 'dehydrated' halloysites display d_{001} reflections that range from 9.98 to 10.08 Å for expanded layers and from 7.19 to 7.34 Å for collapsed layers (T-8 and T-12, Figure 4). 'Hydrated' samples expanded slightly more with FM intercalation when compared to similarly FM-intercalated 'dehydrated' samples (T-8FM and T-12FM in Figure 5, 10.2 Å and 9.8 Å, respectively). DMSO intercalation generally resulted in a slightly greater expansion when compared to FM (T-8FM and T-8DMSO in Figure 5, 10.2 Å and 10.6 Å, respectively). The *b* dimension (measured using d_{060}) for all halloysites ranges from 8.920 to 8.926 Å.

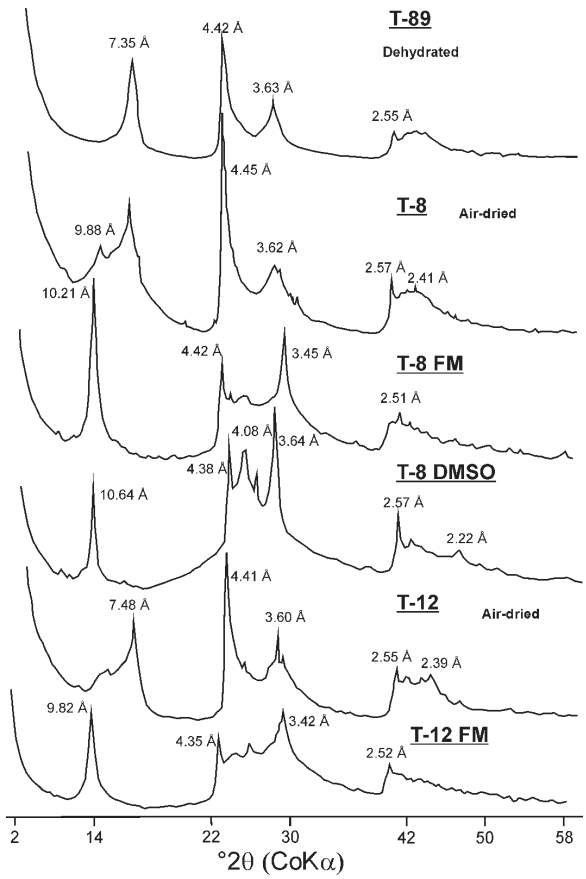

Figure 4. Representative XRD patterns of halloysite samples in the air-dried state (T8), treated with formamide (T8-FM) and dimethyl sulfoxide (T8-DMSO) to distinguish kaolinite and halloysite. Samples were collected from the southern halloysite mine. T-89 was dehydrated in an oven at 60ºC for 2 h. The vertical scale is in relative counts/s.

Alunite lattice parameters were indexed from XRD data (Figure 5), using ZnO as an internal standard that was previously indexed using the US National Institute of Standards and Testing standard reference material (SRM) 640b (Si). Indexing with seven lines from alunite produced the following cell parameters: a = 6.995 Å, c = 17.195 Å and cell volume 728.631 $Å^3$, which is similar to those of synthetic alunite groups (Stoffregen *et al.*, 2000). Coexisting in the alunite XRD data are small peaks at 2.80, 2.70 and 2.63 Å, which are consistent with the presence of a calcium phosphate phase. Some samples show minor amounts of jarosite with diagnostic peaks at d_{101} = 3.08 Å, d_{021} = 3.11 Å, and d_{012} = 5.10 Å.

FE-SEM studies

The FE-SEM images of incipient alteration stages of andesitic tuffs show tubular halloysite morphologies, thus suggesting the direct formation of halloysite as a result of alteration of feldspar (Figure 6a,e). Spheroidal halloysite (diameters ranging from 80 nm to 200 nm) occurs on the edges of altered mica flakes and grows outward into open pore space (Figure 6c,d,f,g,h). Elongate stubby forms are found lying parallel to basal mica surfaces. These forms are variable in size, ranging from 300 to 700 nm long and ~100 nm wide. The growth of more tubular-like halloysite appears to initiate from the edges of feldspathic minerals in spherical form, and then to grow into a stubby morphology.

In the central faulted/altered regions, tubular halloysite morphology is more common. Halloysite particles grow inside small holes in the planar surfaces of vestigial feldspar minerals. The outer diameter of the 'hydrated' halloysite tubes ranges from 60 nm to 100 nm (Figure 7a,b). The 'dehydrated' halloysites are ~170–180 nm (Figure 7c,d). Open-ended tubes (Figure 7g,h) are found in the 'hydrated' halloysites,

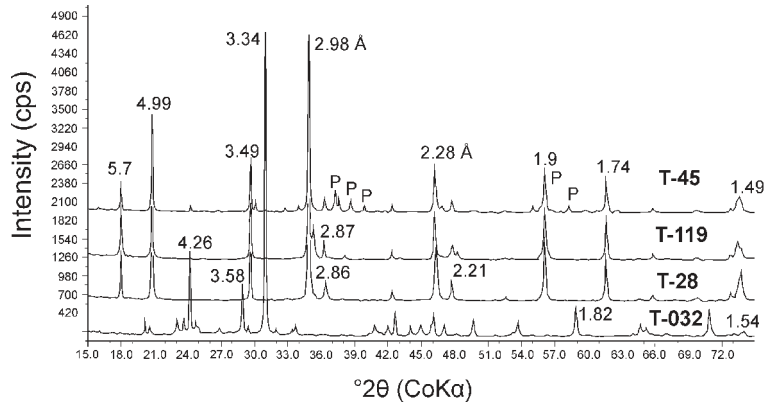

Figure 5. Representative XRD patterns of alunite samples from the northern (T-28 and T-45) and southern (T-032 and T-119) mines. T-45 shows the Ca apatite-richest alunite sample. T-032 displays the presence of jarosite. P = phosphate, A = alunite and J = jarosite.

and closed-end tubes (Figure 7e,f) in the 'dehydrated' halloysites. Pyrite cubes of 0.1−1 mm (not shown) are commonly disseminated amongst these fault clays.

The Cyro-SEM feezing appears to have caused a surface cracking artifact, which is observed as a quasi-hexagonal pattern on platy halloysite flakes and tubular halloysites (Figure 8a,b,c). The Cryo-SEM-prepared samples have outer tube diameters that range from about 80 to 180 nm (Figure 8b), which are larger than the same samples prepared without the freezing step. The cause of these cracks is not clearly understood. One possibility is that the outer layer of tubes crack after the freezing process at −100ºC. Water molecules inside the tube may freeze into an ice structure, expand, and exert outward radial forces. The inner dimensions of the halloysite tubes are ~30 nm. Assuming each water molecule is ~0.15 nm, then there is enough room for 200 molecules across. The volume change associated with the phase transformation from liquid H_2O to solid is ~+10%, thus causing the cracking.

Alunite crystals have distinct rhombohedral form (Figure 9) with dimensions of ~3−5 μm along their edges. The roughened surface morphology suggests a secondary dissolution episode whereby the pore-water compositions may have changed, perhaps as a late-stage weathering effect.

HRTEM studies

The HRTEM observations show that almost all halloysites have a hollow interior. Based on electron density contrast they can be grouped into two populations. The first includes long and continuous hollow tubes with open ends (Figure 10). The outer and inner diameters of these long tubes average ~100 nm and 30 nm, respectively. The second group displays short, discontinuous and double or multiple hollow halloysite tubes with closed ends (Figure 10). Outer diameters of the short tubes extend to 160 nm and double inner holes are 20 and 30 nm. Tube wall thickness varies from 20 to 40 nm.

End views of the tubular particles by the replica method are shown for samples dominated by 10 Å halloysite and 7 Å halloysites in Figure 11. End views reveal 'hydrated', ring-shaped tube diameters measuring ~300 nm. Dehydrated spiral-shaped halloysite measures 500 nm. Tube diameters appear widened due to the replica technique which provides ~20 nm thick platinum and carbon coatings on the clay surface. Some crevices exist in the inner part of the deydrated halloysite, while other tubes become segmented into units of considerable thickness upon dehydration. The mechanism for outer-diameter expansion (from 300 nm to 500 nm or 60% change) is related to the rolled structure of halloysite tubes, the cleavage surfaces of which lose the attractive force between the layers. An inherent strain favors expansion when the rolled configuration of halloysite is dehydrated. Kohyama *et al.* (1978) similarly described the expansion mechanism of dehydrated halloysite tubes as being like book pages rolled by hand and which expand upon relaxation of the grip.

Thermogravimetric studies

Thermogravimetric analysis (TGA) and differential thermogravimetric analysis (DTGA) reveal distinct dehydroxylation steps of alunite and halloysite (Figure 12). Hydrated halloysite exhibits an endothermic peak at ~50ºC, which is lost hydroscopic and interlayer water. Halloysite samples collected near the limestone contact occasionally contained gibbsite which is displayed as a 250ºC endothermic peak. The hydroxyl units of halloysite lost at ~430ºC constitute 11−12 wt.% (after accounting for adsorbed water loss and gibbsite mass). The TGA did not resolve weight-loss differences between 'hydrated' and 'dehydrated' forms at 430ºC.

Five distinct regions of weight loss (endothermic peaks) are observed in the alunite DGTA curve. These data are not commonly analyzed in the clay literature, therefore we provide an interpretation in the steps below, which are based on the work of Slansky (1973), Pysiak and Glinka (1981), Küçük and Gülaboğlu (2002) and Rudolph *et al.* (2003). Removal of initial hydroxyl water in alunite occurs at ~500ºC. Remaining SO_4 is lost during four complex structural changes with endotherms

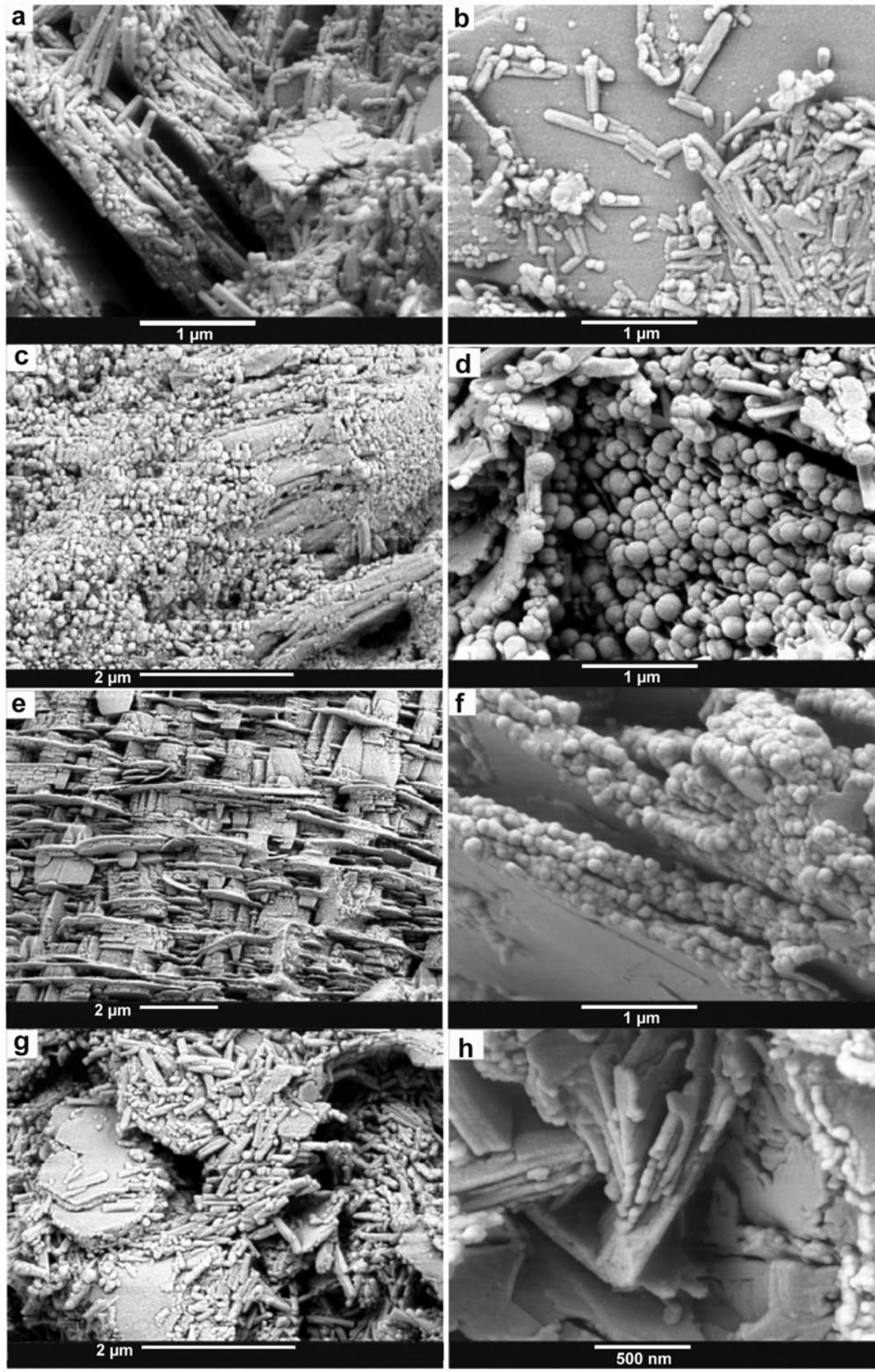
a
1 µm
b
1 µm
c
2 µm
d
1 µm
e
2 µm
f
1 µm
g
2 µm
h
500 nm

at ~610, 670, 740 and 830ºC. These steps correspond to the loss of water through dehydroxylation, and sulfur through sulfate breakdown.

Step 1 (500ºC):

$$KAl_3(SO_4)_2(OH)_6 = KAl(SO_4)_2 + 3H_2O + \alpha\text{-}Al_2O_3$$

Step 2 (610ºC):

$$KAl(SO_4)_2 = \tfrac{1}{2}K_2SO_4 + \tfrac{1}{4}Al_2(SO_4)_3 + \tfrac{1}{4}\alpha\text{-}Al_2O_3 + \tfrac{3}{4}SO_3$$

Step 3 (670ºC):

$$\tfrac{1}{4}Al_2(SO_4)_3 = \tfrac{1}{8}Al_2(SO_4)_3 + \tfrac{1}{8}\alpha\text{-}Al_2O_3 + \tfrac{3}{8}SO_3$$

Step 4 (740ºC):

$$\tfrac{1}{2}K_2SO_4 + \tfrac{1}{8}Al_2(SO_4)_3 = \tfrac{1}{4}K_2SO_4 + \tfrac{1}{4}K_2O + \tfrac{1}{8}\alpha\text{-}Al_2O_3 + \tfrac{5}{8}SO_3$$

Step 5 (830ºC):

$$\tfrac{1}{4}K_2SO_4 + \tfrac{3}{2}\alpha\text{-}Al_2O_3 = \tfrac{1}{4}K_2O + \tfrac{3}{2}\gamma\text{-}Al_2O_3 + \tfrac{1}{4}SO_3$$

Weight losses at ~500ºC observed for alunite-dominated samples ranged between 14.2 and 16.3%. Using the ideal formula of alunite ($KAl_3(SO_4)_2(OH)_6$), weight loss for step 1 is 13.0 wt.%. The second step observed over the range 550–650ºC with the maximum of ~610ºC, has observed values that range from 7 to 10.2 wt.%. The calculated weight loss for step two is 14.5%. The third step is a sharp desulfidation peak that occurs in the region 665–675ºC, with observed values that range from 6.5 to 11.9%. The calculated weight loss for step three is 7.2%. The fourth step is observed at 735–740ºC with weight loss values of 5.2 to 5.5%. The calculated loss is 12.1 wt.%. The final step, observed at ~830ºC, has values of 1.5–5.3 wt.%. The calculated loss for step five is 4.8 wt.%. A total of 51.7% weight is calculated from the ideal alunite formula, whereas the sum of the observed averages for each step is 41.8%. This latter observed value is slightly less than the loss-on-ignition (LOI) average of ~45% seen in the elemental studies of alunite-rich samples (see below). The disagreement between the observed and theoretically calculated weight-loss values is attributed to instrumental effects and the presence of accessory phosphate phases and isomorphous substitutions (such as Na_2O, Fe_2O_3, P_2O_5, trace and rare earth elements) in the alunite structure (see results below). These factors result in pathways of the thermal breakdown not included in the elementary reactions as idealized above.

When the DTA results for alunite are compared with the results of DTGA, different endothermic temperatures are observed. Figure 13 shows three curves for alunite (b, c and d), which exhibit sharp endothermic peaks at 535ºC and ~800ºC, and two exothermic peaks at ~703–740ºC and ~930–1000ºC. The first endothermic reaction is related to the expelling of water molecules and the second endothermic reaction is due to desulfurization. The exothermic peaks show a gain in oxygen from a closed atmosphere while SO_2 was releasing from the system, with the final products probably being $K_2O + Al_2O_3$. The first step is assigned to the decomposition of the alunite structure to alkali aluminum sulfate [$KAl(SO_4)_2$] and Al_2O_3, while the hydroxide is released as water. Rudolph *et al.* (2003) suggested the formation of the phase $K_3Al(SO_4)_3$ appearing at 770ºC as an exothermic peak. It is likely that this phase appeared at 740ºC with small amount of α-Al_2O_3 in our samples. Cielsa and Rudnicki (1993) demonstrated a Ca phosphate decomposition stage at ~700ºC, which is near to the 710ºC endotherm. This is consistent with XRD and elemental data showing the presence of a minor co-existing Ca phosphate phase. The DTGA gives lower thermal breakdown temperatures than DTA (this also seen in halloysite samples), which is probably due to the difference in heating rates and the closed *vs.* open system conditions. These curves are intended to serve as a basis for future comparisons amongst alunites from other deposits.

Elemental and mineral analysis of unaltered volcanics

Hand-specimen and XRD study of the unaltered tuffs reveal that they consist of devitrified glass and pumice fragments, with small phenocrysts of quartz, feldspars and biotite. Other unaltered volcanic flows contain variable abundances of plagioclase, orthopyroxene, hornblende and biotite phenocrysts. Elemental data for the unaltered volcanics are available in Table A1 (www.clays.org/journal/JournalDeposits.html). The Zr/TiO_2 *vs*. Nb/Y volcanic rock classification of Winchester and Floyd (1977) indicate that unaltered rocks fall mostly within the andesite-trachyandesite field and have a subalkaline composition. Si-Na-K classification of the same rocks indicate continuous compositions ranging from basaltic andesite to rhyolite.

The normalized mid-oceanic ridge basalt (N-MORB) and average of bulk continental crust (ABCC) values (Taylor and McLennan, 1985) were selected to normalize trace element and *REE* patterns (Figure A2 and Table A1: www.clays.org/journal/JournalDeposits.html). ABCC normalization allows for the assessment of enriched and depleted elements resulting from hydrothermal alteration and/or weathering. The significant features of the andesites are: (1) enrichment

Figure 6 (*facing page*). Field emission scanning electron micrographs (FE-SEM) of tubular, stubby, and spheroidal halloysite morphologies occurring in altered samples from the southern halloysite mine. (a) Spheroidal and stubby (short-tube) morphologies growing on the edges of mica flakes. (b) 0.2–0.3 μm stubby halloysites on feldspar. (c) Incipient formation of halloysite on feldspar grains. (d) More magnified image of spheroidal halloysite morphologies with sizes ranging from 0.07 to 0.2 μm. (e) Early-stage alteration of andesitic tuffs displaying how feldspar grains modify during dissolution. (f) Spherical halloysite on the edges on feldspar grains with diameters of <0.1 μm. (g) As feldspar passes through to sericitization-type alteration, the abundance of stubby halloysites increases and they become more common on feldspar grain surfaces. (h) Early-stage spheroidal morphology growing on the edges of feldspar grains.

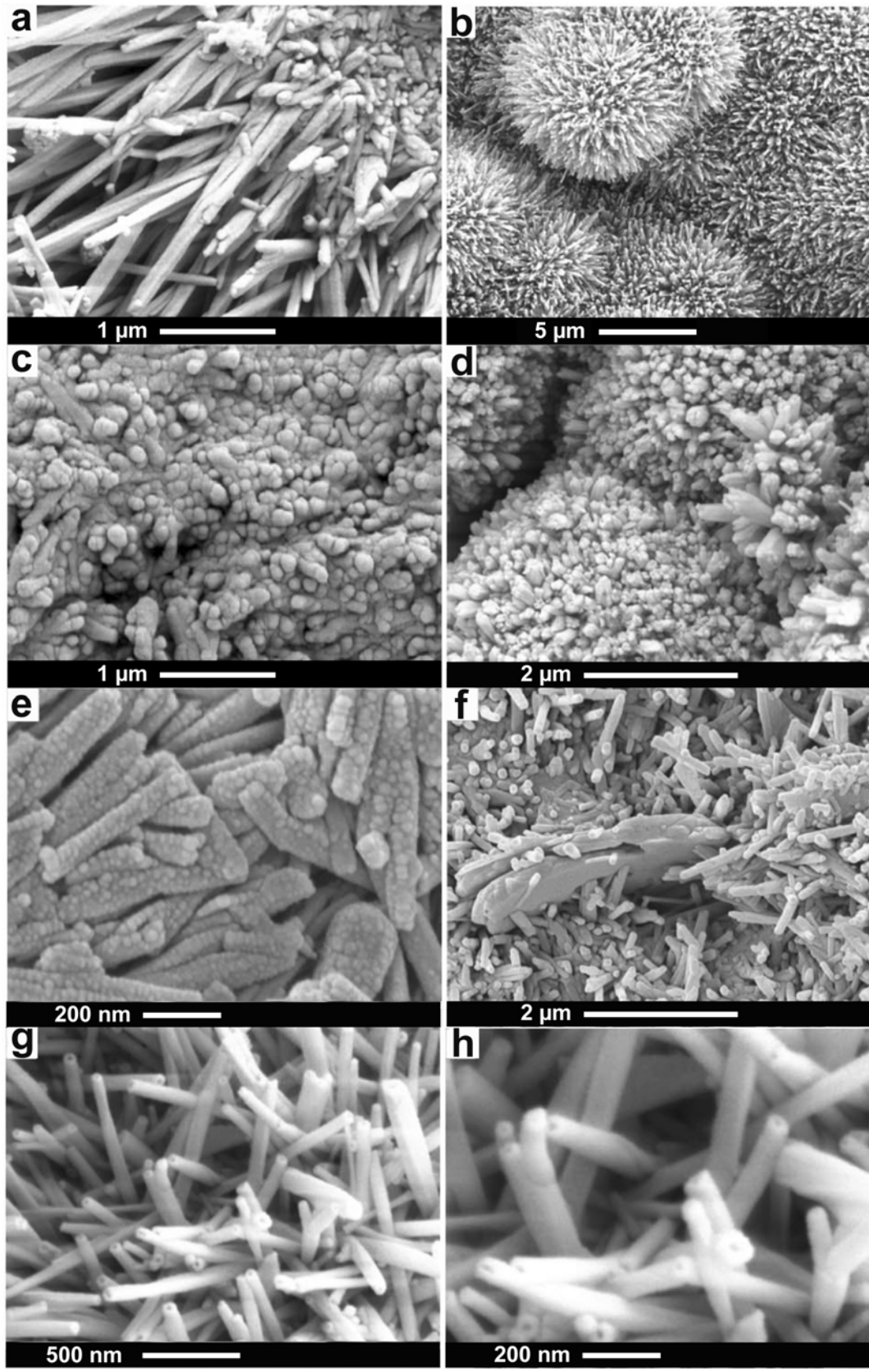
a
1 µm
b
5 µm
c
1 µm
d
2 µm
e
200 nm
f
2 µm
g
500 nm
h
200 nm

of LILE (light ion lithophile elements: Rb, Ba, K, Sr, Th) over *LREE* and *MREE*, resulting in high (Ba/La)*n* (2.8−5.5), (K/La)*n* (0.3−2.4) and (Th/La)*n* (2−15.6) ratios; (2) depletion of HFSE (high field strength elements: Ta, Nb, Zr, Ti) with respect to neighbouring LILE and *REE*, yielding low (Nb/Ba)*n* (0.01−0.03), (Nb/La)*n* (0.05−0.5), (Ti/Sm)*n* (0.14−0.36) and (Zr/Sm)*n* (0.4−2.6) ratios and (3) fractionation among LILE generating pronounced positive Sr and Pb anomalies relative to *MREE*. N-MORB values for the unalterd andesites (Figure A2: www.clays.org/journal/JournalDeposits.html) compare favorably with the magmas formed in an arc-type or in the post-collisional setting, such as those observed in the central zones of Andean volcanics (Thorpe *et al.*, 1982; Davidson *et al.*, 1991; Walker *et al.*, 1991; Thorpe *et al.*, 1984; Harris *et al.*, 1994). The high La (22−204), Ce (40−336), Th (12−30) and Pb (7−88) contents (ppm) are also consistent with the post-collisional hybrid origin (Pearce *et al.*, 1990; Harris *et al.*, 1986).

Most altered volcanics display an apparent enrichment in LILE and a depletion in HFSE indicating that they retain the magmatic-arc volcanic origin (Figure A3: www.clays.org/journal/JournalDeposits.html). The co-enrichment of K, Rb, Th, Ba and to a lesser extent of Sr and *LREE* (Table A1: www.clays.org/journal/JournalDeposits.html) suggest that there is a significant crustal contribution in the mantle-derived magma (Karacık and Yılmaz, 1998).

Elemental and mineral analyses of alteration products

Core-to-rim Fe staining is a common feature in larger exfoliations of altered andesitic tuffs. Pyrite, realgar, cinnabar, orpiment, azurite, bornite, chalcopyrite, psilomelane, hematite, gypsum and other clays are sometimes associated with halloysite and alunite mineralization. Pyrite is mostly concentrated within the fault clays with small amounts of chalcopyrite. Arsenic and Cu sulfides are irregularly distributed in very small discontinuous bands in the clay body. Very thin and discontinuous gibbsite-rich zones occur between halloysite and large limestone blocks. The limestone blocks range from 3 m^3 to 5 m^3 in size and are sometimes surrounded by 10−20 cm thick Fe and Mn hydroxide (goethite and psilomelane) bands. Also, gypsum bands are found on the surface of limestone blocks and infilling micro fractures in the blocks to a depth of ~20 cm.

Halloysite-rich samples show large depletions in Fe, Mg, Ca, Na, K and Ti ($\%\Delta_i$ range = −26 to −100%) and moderate depletion of Si is observed ($\%\Delta_{Si}$ range = −30 to −72%). The latter value indicates a partitioning of silica from silicate dissolution to form the halloysite and the transport of Si away from sites. The texture of primary quartz in the volcanic rocks appears to be conservatively retained. This primary quartz positively influences the $\%\Delta_{Si}$ alteration index values, which means that in some cases the $\%\Delta_{Si}$ values do not entirely reflect the extent of silica loss from dissolution of other framework silicates (*i.e*. feldspars and micas).

Tables A2 and A3 (www.clays.org/journal/JournalDeposits.html) contain elemental analysis of altered materials from the two deposits. Elemental analysis of 'hydrated' and 'dehydrated' halloysite-dominated samples produce similar abundances because the method pre-dries samples at 110ºC. Small variations in the elemental analysis can, in part, be attributed to the relative abundances of minor mineral phases, such as quartz, aluminosilicates, goethite, gibbsite and smectite. Large difference trends in elemental composition are attributed to mass losses and gains associated with hypogene and hypergene events.

Major elemental analyses of alunite-rich materials from the two deposits (T102−T108) are consistent with XRD and TG analyses which indicate that the samples contain ~6−8 wt.% phosphate as a separate phase. Alteration indices for alunite-rich samples show nearly 100% depletion of Si, Fe, Mg and Ti ($\%\Delta_{Si,Fe,Mg,Ti}$ ranges from −87 to 99%). Moderate depletion of K, Ca and Na occurs ($\%\Delta_{K,Ca,Na}$ ranges from −4 to −98%), with slightly greater retention in phosphate-bearing alunites from the north site, when compared to the south site. Net gains in P ($\%\Delta_P$ range = −16 to 690%) are seen with the largest $\%\Delta_P$ index observed at the northern mine (Table A4: www.clays.org/journal/JournalDeposits.html). Net gains are generally brought about by volume reduction, as demonstrated by the highly deformed and contorted nature of the Turplu deposits in the fault zones. Field reconnaissance however, has not yet noted a major difference in the amount of deformation between the two deposits.

The alunite supergroup, having rhombohedral structure with $a \approx 7$ Å and $c \approx 17$ Å, can have more than 40 minerals with the general formula, $AB_3(XO_4)_2(OH)_6$, where *A* is a monovalent or divalent large ion (K, Na, NH_4, H_3O, Ca, Ba, Pb, Bi, *REE*), *B* is trivalent Al^{3+} or Fe^{3+} and *X* is S^{6+}, As^{5+} and P^{5+} (SO_4, PO_4, AsO_4) (Jambor, 1999; Rattray *et al.*, 1996). Alunite samples are enriched in *REE* contents with respect to the parent rocks

Figure 7 (*facing page*). Fractured surface of aggregate FE-SEM images from the Turplu southern mine showing tubular morphology. (a) Gradation from stubby to long-tube morphology in free space. (b) Large, ~10 μm, diameter spherical bundles of halloysite tubes growing into free space. (c) Halloysite from a very altered parent mineral. (d) ~5 μm spherical mass presumed to be early stages of elongate tubes. (e) ~200−300 nm long halloysite tubes displaying possible acid sulfate alteration on the mineral surfaces. (f) ~0.5−1 μm long halloysite growing in free space. (g) Hollow tubular morphology representing a later stage of mineral growth. (h) More magnified view (200 nm × 40 nm) of hollow tubular halloysites.

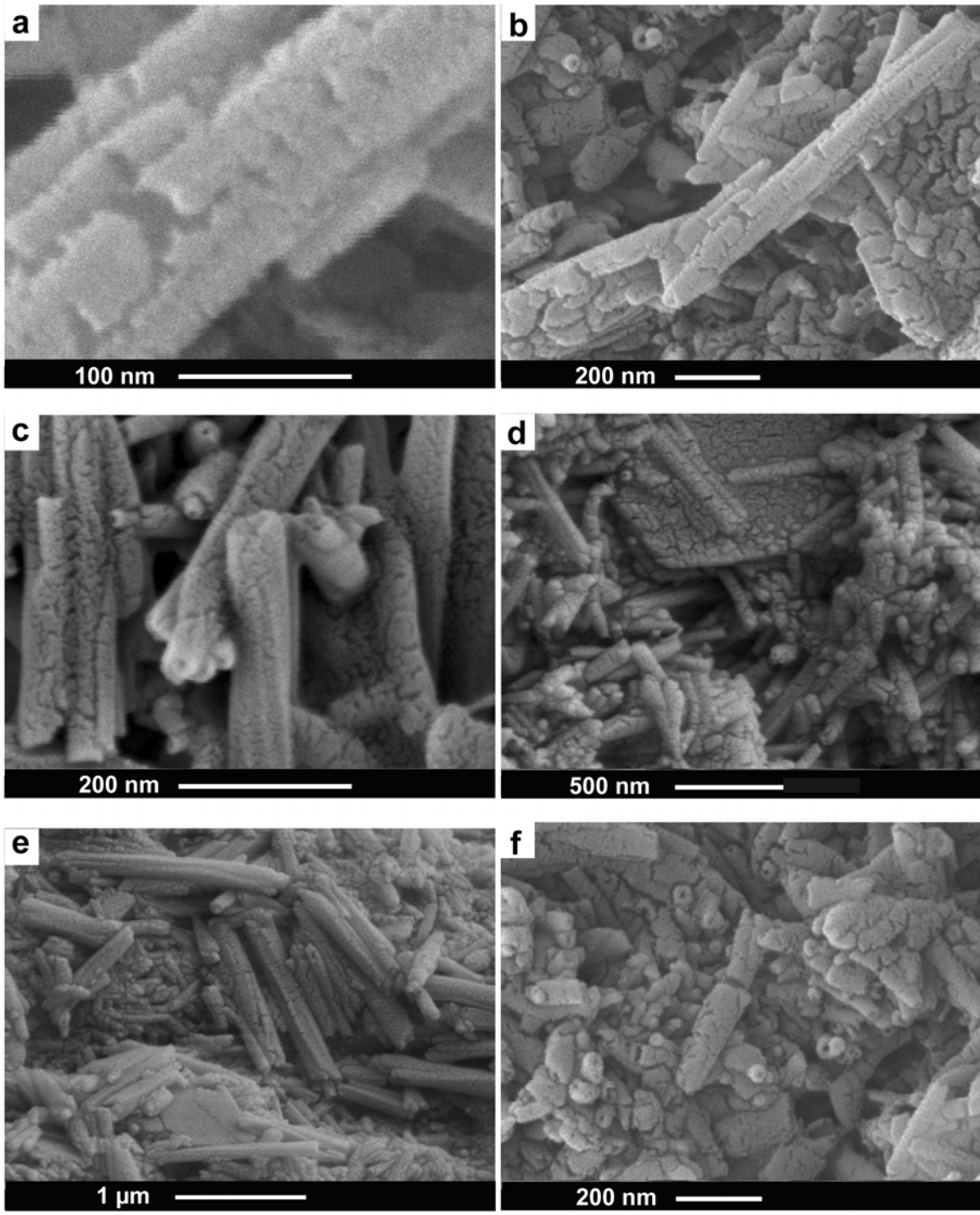

Figure 8. Cyro-FE-SEM images showing the original morphology of hydrated halloysites without the effects of dehydration. These studies show the actual dimensions of the tubular structure in hydrated halloysite samples. Surface layers are cracked due to volume expansion at −100ºC. The tubular minerals range from 0.2 to 1 µm long and from 80 to 100 nm in diameter. Samples are from the southern halloysite mine and were kept hydrated inside a water-filled cap. (a, b and c) show in detail morphologies of hydrated tubular halloysites; (c) tubes with open-ends; (b and d) cracks on the surface of hexagonal halloysites together with tubular structure <0.5 µm long. (e) Tubular structures ~1 µm long on the hexagonal structure. (f) Open-end halloysite morphology and transition from stubby to long-tubular textures.

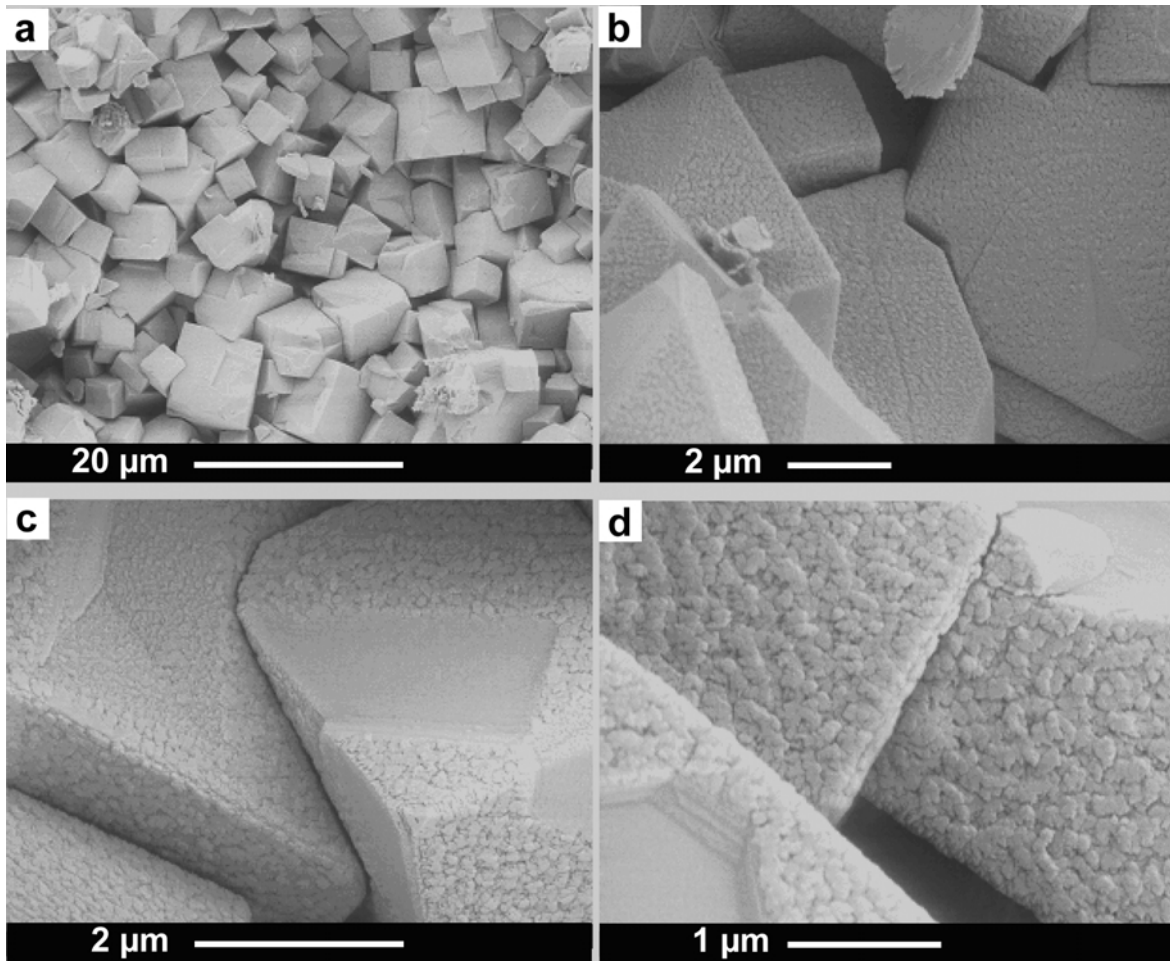

Figure 9. FE-SEM images of alunite from the northern alunite mine. (a) Low-magnification view of alunite morphology displaying rhombohedral structure. (b) Alunites showing some dissolution marks on their surfaces due to possible late-stage acid sulfate alteration or meteoric weathering. (c and d) Casts of step growth features at contact points during mineral growth and subsequent dissolution textures on surfaces exposed to pore space.

(Figure A4: www.clays.org/journal/JournalDeposits.html). Alunite nodules (4–6 cm) from the southern mine are more enriched in *REE* than nodules from the northern mine. Both deposits show enrichments of *LREE*s relative to the *MREE*s, while the distribution of *HREE*s is invariant. The enrichment patterns of trace element and *REE*s are much greater in alunites than in halloysites, which suggests that there are geochemical differences between the northern and southern mines. This is demonstrated in the linear trend observed between total *REE* and phosphate contents in alunites (Figure 14). The slightly smaller P gains in the southern mine suggests that they may have experienced a slightly different alteration history from the northern mine.

DISCUSSION

Hydrothermal alteration along fault zones

The genetic distinction between alunite and aluminum-phosphate-sulfate (APS) minerals containing hypogene and supergene kaolinization has been examined on the basis of Zr *vs.* TiO_2, Cr + Nb *vs.* Ti + Fe and Ba + Sr *vs*. Ce + Y + La (Dill *et al.*, 1997; Dill, 2001). The enrichment of S, Ba and Sr is common in kaolin during hydrothermal alteration, whereas Cr, Nb, Ti and La are concentrated mainly during weathering processes (Dill *et al.*, 1997). This was demonstrated with Peruvian kaolin deposits where central zones of the Andean mountains also have calc-alkaline volcanism. Dill *et al.* (1997) found that hypogene kaolin deposits in Peru are enriched in S and P due to the presence of alunite and assume that the source of P is in phosphate-bearing minerals that appear during the later stage of magma differentiation. Zr and Ti are relatively immobile under near-surface conditions, so they can be used as conservative elements to indicate the degree of weathering (Railsback, 2003; Yau *et al.*, 1987). Halloysite samples from both mines follow an almost linear Zr *vs.* TiO_2 trend and strongly suggest a hypogene origin when compared to the Peruvian kaolins (Figure 15). The

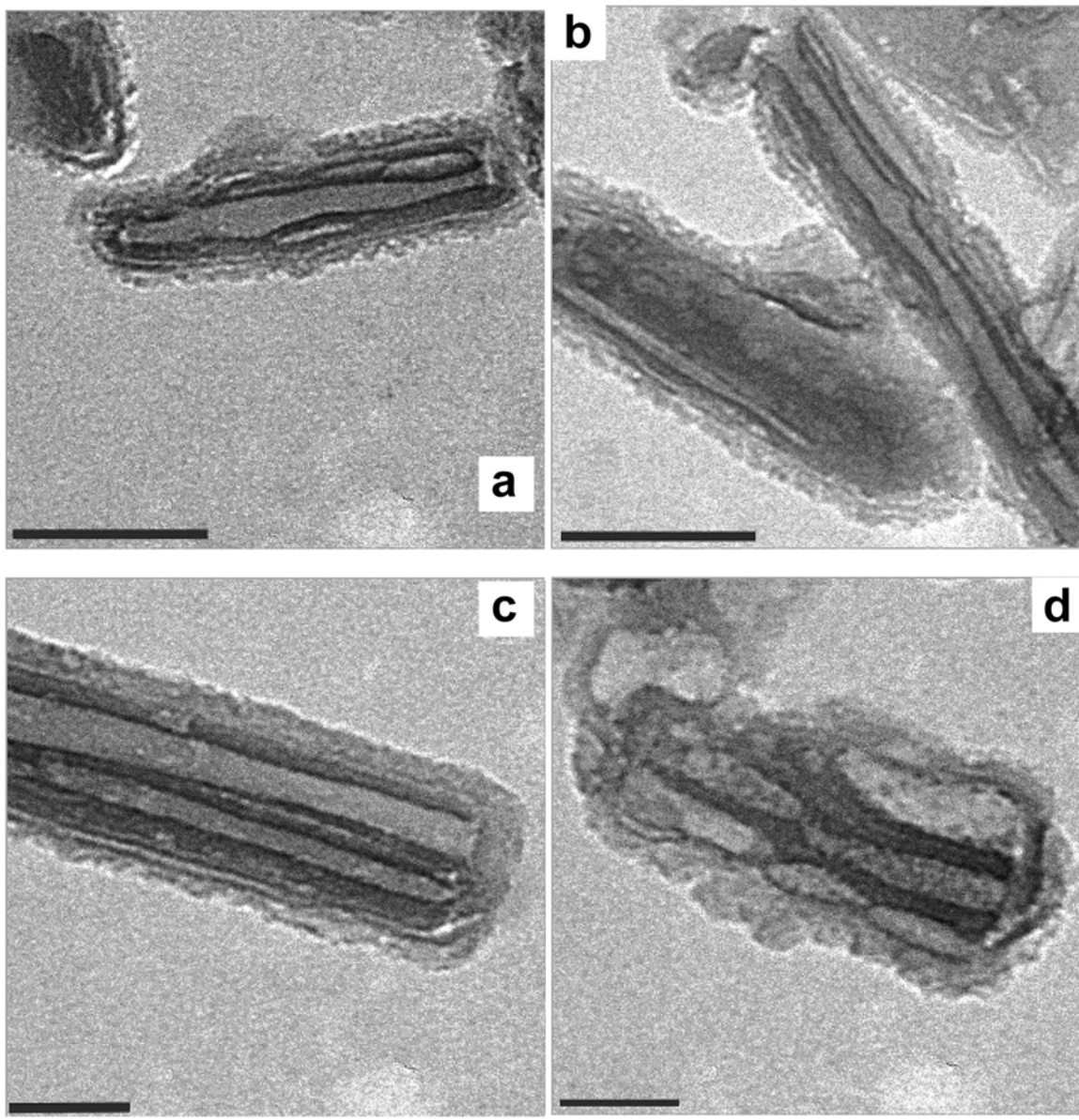

Figure 10. HRTEM studies present electron density contrast, which provides greater resolution at which to examine the inner and outer diameters of the tubular morphologies. Dehydrated tubes are not uniform or straight (a, b, c). Inner tube dimensions can be discontinuous. Hydrated halloysites (d) have more uniform, continuous and straight inner-tube dimensions. Scale bars = 100 nm.

northern mine displays slightly more enrichment in Zr and TiO_2. The distinction between hypogene, supergene and mixed-type sources based on Dill *et al.*, (1997) also suggests that Ba and Sr mostly occur in hypogene deposits and Ce, Y and La are concentrated in bauxite and supergene deposits. Turplu may differ from the Peruvian kaolins in that the groundwaters migrating through much of Biga Peninsula are traveling through the Permian limestone as a carrier bed (Yalçın, 1997). This is supported by studies of the Kazdağı massif Turplu-Gönen-Ekşidere geothermal fields, which are located ~100 km to the east (Yalçın, 1997).

Weathering overprinting

The element depletion pattern within the core stone (as tracked by the alteration indexes) indicate that both volcanic rock and its alteration products have undergone surface weathering (Figure 16). Mg, Ca, Na and K (and other group IA and IIA, Table A2: www.clays.org/journal/JournalDeposits.html) are almost entirely depleted. Si undergoes depletion towards the edge, with the exception of the middle sample (T-66), which contains smectite (XRD data not shown). The pattern of greater Fe depletion at the edge to lesser depletion in the core is attributed to the mobilization by subsurface bacteria. This is presumably

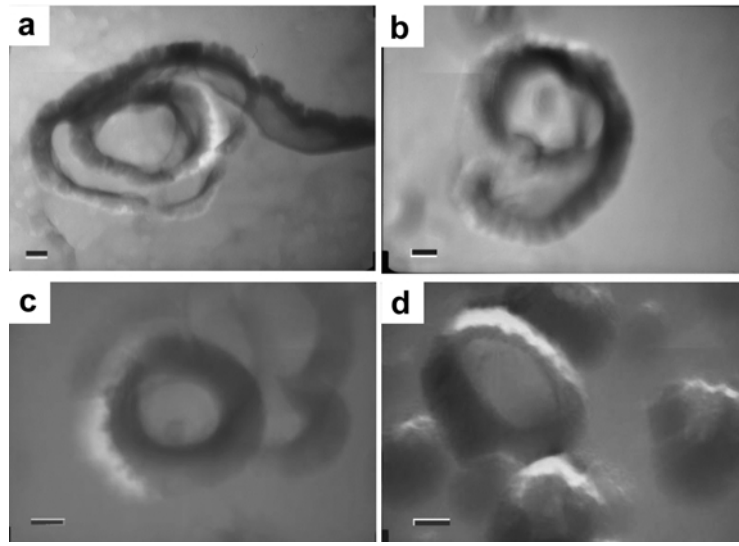

Figure 11. HRTEM of replica of freeze-fracture dehydrated (a,b – spiral shape) and hydrated (c,d – donut shape) halloysites. Samples from the southern halloysite mine. Scale bars = 100 nm.

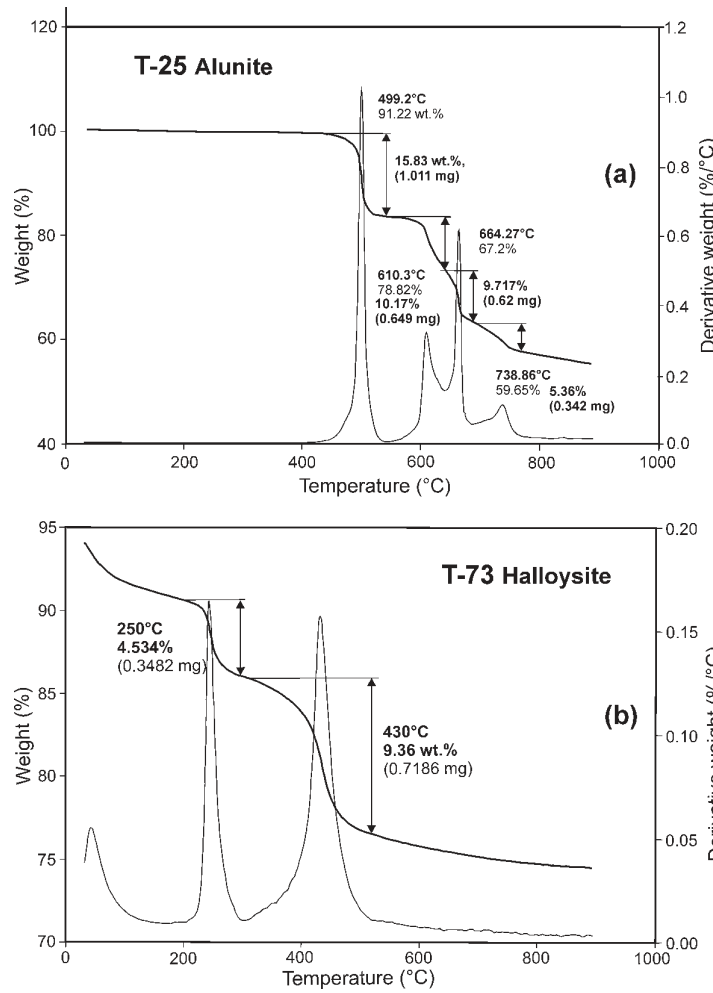

Figure 12. DTG and TG analyses of alunite (a) and halloysite (b) with endothermic peaks at ~50ºC and 430ºC and gibbsite endothermic peak at 250ºC. The samples were run in a helium atmosphere.

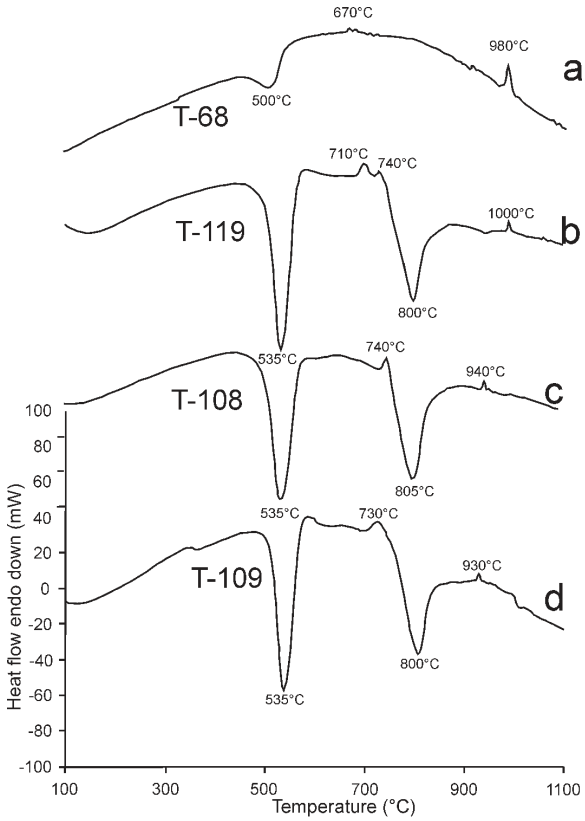

Figure 13. DTA of alunite samples. The samples were run in an argon atmosphere.

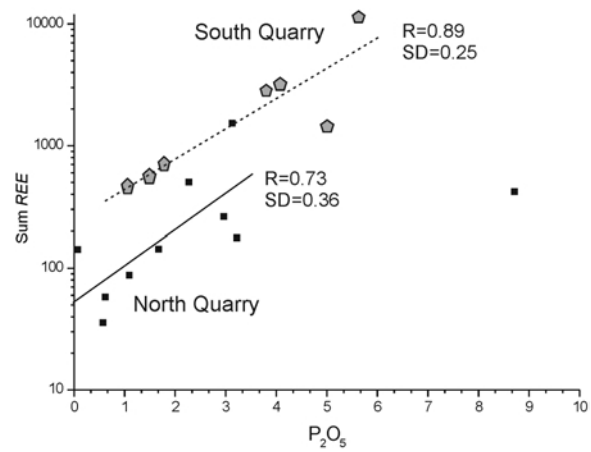

Figure 14. Comparison of the northern and southern mines is based on *REE* and P content. The solid and dashed lines represent best-fit linear trends to the respective data sets. R = correlation coefficient and SD = standard deviation.

done by the combined action of Fe chelating siderophores and slowly infiltrating groundwaters as proposed by Hurst and Pickering (1997) and Shelobolina (2000). Iron is oxidized to hematite and goethite during hydrothermal alternation. The greater solubility of hematite relative to goethite under the recent ambient geochemical conditions further leads to the dissolution of hematite and subsequent migration through the groundwater system. The net result is the migration of Fe as bacteria reduce and dissolve it and oxygen diffuses in and precipitates in mineral form. The consequence of bacterial Fe dissolution and outward Fe diffusion, inward O_2 diffusion, and crystal growth of ferric hydroxides is manifested in liesigang banding which is common throughout the deposits (*e.g.* Figure 3). Depletion of all major elements and *REE* (except for Al) relative to the local andesite (T-32) occurs in the most weathered and altered halloysite.

Field relations of juxtaposed volcanics and limestone suggests that the mass loss of these components is related to the porous karstic terrain underlying the

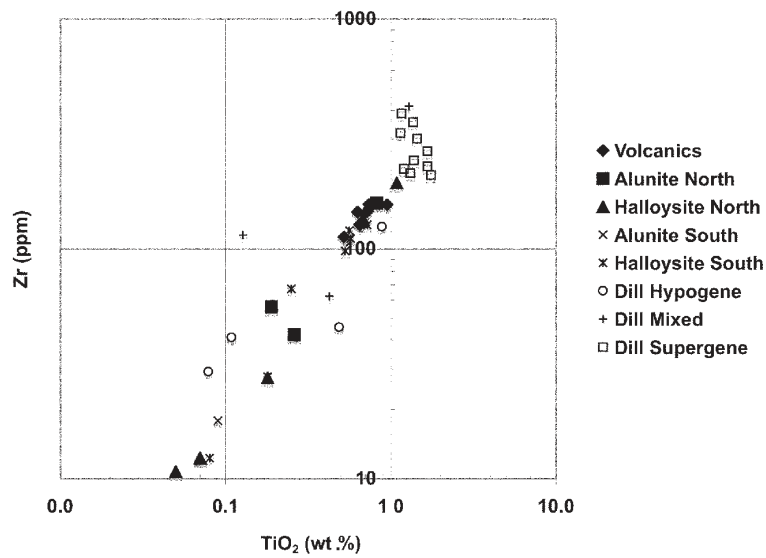

Figure 15. Zr *vs*. TiO_2 plot of halloysite samples from the northern and southern mines. Solid symbols represent hypogene, supergene, and mixed origin of alunite and APS minerals from kaolin deposits in Peru (Dill *et al*., 1997).

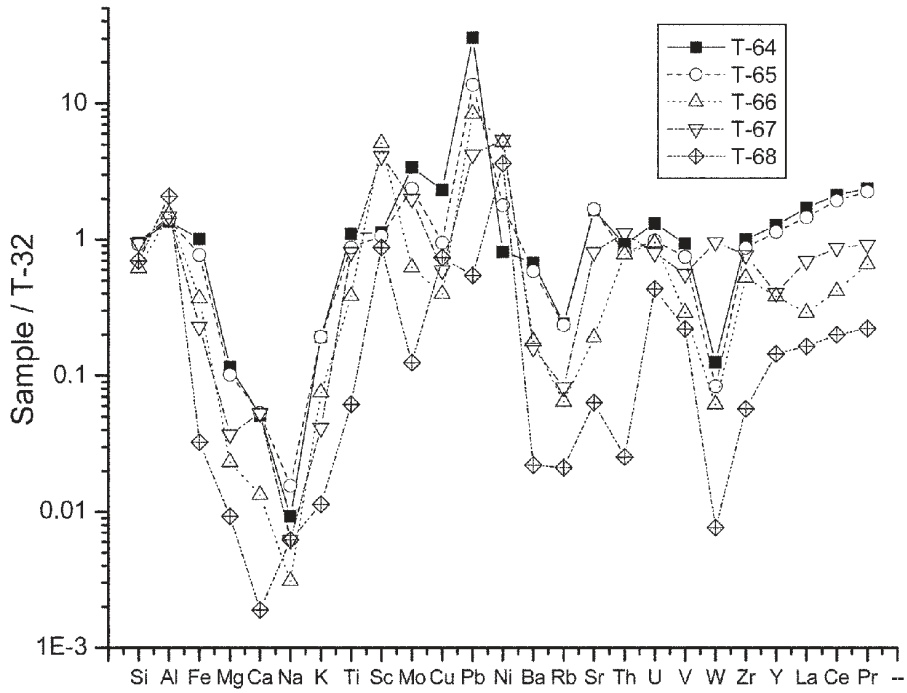

Figure 16. Andesite normalized elemental abundance (sample T-32) patterns from the least altered (T-64) andesitic tuffs to the most altered (T-68) halloysite (Figure 4).

volcanic deposits. The permeable karst facilitates the flux of dissolved components in and out of the fault zones during hydrothermal alteration and continues afterwards during weathering. The slightly smaller P gains in the southern mine suggests that it has experienced less flushing or a lower-grade alteration history when compared to the northern mine deposits.

Mineralogical, chemical and morphological analysis of the Turplu clays indicates that their origins result from three general periods of alteration. These alteration stages include: (1) the period of initial deposition of volcanic tuffs and andesites on top of a previously weathered karstic carbonate terrain; (2) a subsequent period of extensional and strike-slip faulting events and contemporaneous hydrothermal fluid circulation through the faults (*i.e.* hypogene alteration), and (3) a present-day near-surface weathering period (*i.e.* supergene alteration) associated with continued faulting.

CONCLUSIONS

A mineralogical and crystal-chemical study of alunite- and halloysite-rich deposits in the Turplu area of NW Turkey reveals a diverse and a potentially economic clay deposit. The mineral assemblage along fault zones is dominated by halloysite and sometimes alunite. Of the two deposits studied, the northern mine contains more alunite relative to halloysite. Geochemical indices suggest that the northern mine has experienced a slightly greater degree of alteration. Halloysite is found in both hydrated and dehydrated states and assumes a tubular morphology. The TEM and SEM observations are consistent with a model of halloysite dehydration by which the shapes transform from an open-hole tubular morphology to a closed-hole unfurled morphology.

Field relations and mineral relations suggest that these deposits have been influenced by three periods of alteration. The first includes the initial deposition of volcanic tuffs and andesite on the karstic terrain. The second includes a period of hydrothermal alteration (hypogene) contemporaneous with extensional and strike-slip faulting. The third stage includes modern weathering (supergene) and the formation of saprolitic material that is undergoing both plastic and brittle deformation. Hydrothermal alteration is concentrated near the fault zones. Away from the fault zone, much of the andesitic volcanic rocks have been weathered to form a more smectite-rich and kaolinite-bearing alteration assemblage. The contact between altered volcanics and underlying limestones is irregular. Tectonic deformation has mixed the contacts, such that limestone blocks have been entrained into parts of the alteration zones. Gibbsite and gypsum are common weathering products associated with limestone block inclusions.

The timing and temperatures of this proposed paragenetic sequence cannot be addressed with the mineralogical, morphological and elemental information presented here. These aspects can be studied through a parallel study of the same samples using stable and radiogenic isotopic methods. Preliminary studies have been initiated (Schroeder *et al.*, 2004a, 2004b) and a more complete assessment will be presented.

ACKNOWLEDGMENTS

This research was made possible with the support of TÜBİTAK-YDABÇAG Project No: 101Y137 (Ö.I. Ece) and NSF INT-0138023 (P.A. Schroeder). Additional support was obtained from the Istanbul Technical University Research Fund (No: 30345) (Ö.I. Ece). We are grateful to Drs John P. Shields and Mark A. Farmer (UGA -Center for Ultrastructural Research) for the FE-SEM, TEM and HRTEM studies. We are also grateful to Mustafa Bal and İlhami Tezcan of KALEMADEN Corp., and Yüceer Göver, Dr İhsan Bozdoğan and Ali Uygun of ESAN Eczacıbaşı Corp. for their logistical assistance and accommodation during fieldwork. We thank Ray Ferrell and Helen Lever for acting as reviewers.

REFERENCES

Altaner, S.P., Ylagan, R.F., Savin, S.M., Aronson, J.L., Belkin, H.E. and Pozzuoli, A. (2003) Geothermometry, geochronology, and mass transfer associated with hydrothermal alteration of a rhyolitic hyaloclastite from Ponza Island, Italy. *Geochimica et Cosmochimica Acta*, **67**, 275–288.

Altunkaynak, Ş. and Yılmaz, Y. (1998) The Mount Kozak magmatic complex, Western Anatolia. *Journal of Volcanology and Geothermal Research*, **85**, 211–231.

Altunkaynak, Ş. and Yılmaz, Y. (1999) The Kozak Pluton and its emplacement. *Geological Journal*, **34**, 257–274.

Bozzola, J.J. and Russell, L.D. (1999) *Electron Microscopy. Principles and Techniques for Biologists.* Jones and Bartlett Publishers, Boston, Massachusetts, USA, 670 pp.

Churchman, G.J. (1990) Relevance of different intercalation tests for distinguishing halloysite from kaolinite in soils. *Clays and Clay Minerals*, **38**, 591–599.

Churchman, G.J., Whitton, J.S. and Claridge, G.G.C. (1984) Intercalation method using formamide for differentiating halloysite from kaolinite. *Clays and Clay Minerals*, **32**, 241–248.

Ciesla, K. and Rudnicki, R. (1993) Thermal-decomposition of $Ca_{10}(PO_4)_6(OH)_2$ at ambient-pressure in air and in nitrogen. *Polish Journal of Chemistry*, **67**, 2103–2111.

Davidson, J.P., Harmon, R.S. and Worner, G. (1991) The source of central Andean magmas: some considerations. Pp. 233–243 in: *Andean Magmatism and its Tectonic Setting* (R.S. Harmon and C. Rapela, editors). Geological Society of America Special Paper, **265**.

Dill, H.G. (2001) The geology of aluminium phosphates and sulphates of the alunite group minerals: a review. *Earth Science Reviews*, **53**, 35–93.

Dill, H.G., Bosse, H.R., Henning, K.H., Fricke, A. and Ahrendt, H. (1997) Mineralogical and chemical variations in hypogene and supergene kaolin deposits in a mobile fold belt, the Central Andes of northwestern Peru. *Mineralium Deposita*, **32**, 149–163.

Dixon, J.B. and McKee, T.R. (1974) Internal and external morphology of tubular and spheroidal halloysite particles. *Clays and Clay Minerals*, **22**, 127–137.

Ece, Ö.I. and Nakagawa, Z. (2003) Alteration of volcanic rocks and genesis of kaolin deposits in Şile Region, northern Istanbul, Turkey. Part II. Differential mobility of elements. *Clay Minerals*, **38**, 529–550.

Freeman, T. (1999) *Procedure in Field Geology*. Blackwell Science, Inc., Malden, Massachusetts, USA, 95 pp.

Genç, C.Ş. (1998) Evolution of the Bayramiç magmatic complex, northwestern Anatolia. *Journal of Volcanology and Geothermal Research*, **85**, 233–249.

Grant, J.A. (1986) The isocon diagram – A simple solution to Gresen's equation for metasomatic alteration. *Economic Geology*, **81**, 1976–1982.

Gresens, R.L. (1967) Composition-volume relationships of metasomatism. *Chemical Geology*, **2**, 47–55.

Harris, N.B.W., Pearce, J.A. and Tindle, A.G. (1986) Geochemical characteristics of collision-zone magmatism. Pp. 67–81 in: *Collision Tectonics* (M.P. Coward and A.C. Ries, editors). Special Publication, **19**, Geological Society, London.

Harris, N.B.W., Kelley, S. and Okay, A.I. (1994) Post-collision magmatism and tectonics in northwest Anatolia. *Contributions to Mineralogy and Petrology*, **117**, 241–252.

Hurst, V.J. and Pickering, S.M. (1997) Origin and classification of coastal plain kaolins, southeastern USA, and the role of groundwater and microbial action. *Clays and Clay Minerals*, **45**, 274–285.

Jambor, J.L. (1999) Nomenclature of the alunite supergroup. *The Canadian Mineralogist*, **37**, 1323–1341.

Joussein, E., Petit, S., Churchman, J., Theng, B., Righi, D. and Delvaux, B. (2005) Halloysite clay minerals – a review. *Clay Minerals*, **40**, 383–426.

Karacık, Z. and Yılmaz, Y. (1998) Geology of the ignimbrites and the associated volcano-plutonic complex of the Ezine area, northwestern Anatolia. *Journal of Volcanology and Geothermal Research*, **85**, 251–264.

Kohyama, N., Fukushima, K. and Fukami, A. (1978) Observation of the hydrated form of tubular halloysite by an electron microscope equipped with an environmental cell. *Clays and Clay Minerals*, **26**, 25–40.

Küçük, A. and Gülaboğlu, M.S. (2002) Thermal decomposition of Saphane alunite ore. *Industrial Engineering and Chemical Resources*, **41**, 6028–6232.

Okay, A.I., Siyako, M. and Burkan, K.A. (1991) Geology and tectonic evolution of the Biga Peninsula, northwest Turkey. *Bulletin of Istanbul Technical University*, **44**, 191–256.

Okay, A.I., Demirbağ, E., Kurt, H., Okay, N. and Kuşçu, I. (1999) An active, deep marine strike-slip basin along the North Anatolian Fault in Turkey. *Tectonics*, **18**, 129–147.

Okay, A.I., Kaşlılar-Özcan, A., İmren, C., Boztepe-Güney, A., Demirbağ, E. and Kuşçu, I. (2000) Active faults and evolving strike-slip basins in the Marmara Sea, northwest Turkey: a multichannel seismic reflection study. *Tectonophysics*, **321**, 189–218.

Pearce, J.A., Bender, J.F., De Long, S.E., Kidd, W.S.F., Low, P.J., Güner, Y., Saroglu, F., Yılmaz, Y., Moorbath, S. and Mitchell, J.J. (1990) Genesis of collision volcanism in eastern Anatolia Turkey. *Journal of Volcanology and Geothermal Research*, **44**, 189–229.

Pysiak, J. and Glinka, A. (1981) Thermal decomposition of basic aluminum potassium sulphate. Part I. Stages of decomposition. *Thermochimica Acta*, **44**, 21–28.

Railsback, B. (2003) Earth scientist's periodic table of the elements and their ions. *Geology*, **31**, 737–740.

Rattray, K.J., Taylor, M.R. and Bevan, D.J.M. (1996) Compositional segregation and solid solution in the lead-dominant alunite-type minerals from Broken Hill, N.S.W. *Mineralogical Magazine*, **60**, 779–785.

Rudolph, W.W., Mason, R. and Schmidt, P. (2003) Synthetic alunites of the potassium-oxonium solid solution series and some other members of the group: synthesis, thermal and X-ray characterization. *European Journal of Mineralogy*, **15**, 913–924.

Schroeder, P.A., Pruett, R.J. and Melear, N.D. (2004a) Crystal-chemical changes in an oxidative weathering front in a middle Georgia kaolin deposit. *Clays and Clay Minerals*, **52**, 212–220.

Schroeder, P.A., Smilley, M.J., Ece, Ö.I. and Wampler, M. (2004b) Sulfur isotope and potassium argon analysis of minerals from the Turplu halloysite mine, Balikesir region, northwest Turkey. *The Clay Minerals Society, 41st Annual meeting*, Richland, WA. Abstract with programs, p. 134.

Shelobolina, E. (2000) Role of microorganisms in development of commercial grade kaolins. Pp. 45–59 in: *Guidebook – Geology of the commercial kaolin mining district of central and eastern Georgia* (J. Elzea-Kogel, S.M. Pickering Jr., E. Shelobolina, J. Yuan and T.M. Chowns, editors). Volume **20**, Georgia Geological Society, Georgia, USA.

Singh, B. (1996) Why does halloysite roll? – A new model. *Clays and Clay Minerals*, **44**, 191–196.

Slansky, E. (1973) The thermal investigation of alunite and natroalunite. *Neues Jahrburch für Mineralogie*, **3**, 124–138.

Stoffregen, R., Alpers, C.N. and Jambor, J.L. (2000) Alunite-jarosite crystallography, thermodynamics and geochronology. Pp. 453–479 in: *Sulfate Minerals* (C.N. Alpers, J.L. Jambor and D.K. Nordstrom, editors). Reviews in Mineralogy & Geochemistry, **40**, Mineralogical Society of America, Chantilly, Virginia and the Geochemical Society, Washington, D.C.

Taylor, S.R. and McLennan, S.M. (1985) *The Continental Crust: Its Composition and Evolution*. Blackwell Scientific, Oxford, UK, 312 pp.

Theng, B.K.G., Churchman, G.J. and Whitton, J.S. (1984) Comparison of intercalation methods for differentiating halloysite from kaolinite. *Clays and Clay Minerals*, **32**, 249–258.

Thorpe, R.S., Francis, P.W., Hammill, M. and Barker, M.C.W. (1982) The Andes. Pp. 187–205 in: *Andean Magmatism and its Tectonic Setting* (R.S. Thorpe, editor). John Wiley & Sons.

Thorpe, R.S., Francis, P.W. and O'Callaghan, L. (1984) Relative roles of source composition, fractional crystallisation and crustal contamination in the petrogenesis of Andean volcanic rocks. *Philosophical Transaction of the Royal Society*, *London*, **A310**, 675–692.

Walker, J.A., Moulds, T.N., Zentilli, M. and Feigenson, M.D. (1991) Spatial and temporal variations in volcanics of the Andean central volcanic zone (26 to 28). Pp. 139–155 in: *Andean Magmatism and its Tectonic Setting* (R.S. Harmon and C. Rapela, editors). Geological Society of America Special Paper, **265**.

Winchester, J.A. and Floyd, P.A. (1977) Geochemical discrimination of different magma series and their differentiation products using immobile elements. *Chemical Geology*, **20**, 325–343.

Yalçın, T.H. (1997) Hydrogeological investigation of Gönen and Ekşidere (Balıkesir) thermal waters (NW Turkey). Pp. 275–300 in: *Active Tectonics of Northwestern Anatolia - The Marmara Poly-Project* (C. Schindler and M. Pfister, editors). vdf, Hochschulverlag AG an der ETH Zürich.

Yau, Y.C., Peacor, D.R. and Essene, E.J. (1987) Authigenic anatase and titanite in shales from the Salton Sea Geothermal Field, California. *Neues Jahrbuch für Mineralogie Monatshefte*, **19**, 441–452.

(*Received 6 August 2004; revised 31 August 2006; Ms. 949; A.E. Ray E. Ferrell, Jr.*)